J. Water Environ. Nanotechnol., 8(1): 1-12 Winter 2023

ORIGINAL RESEARCH PAPER

Synthesis and characterization of iron incoporated metal-organic framework (MOF) photocatalyst in degradation of methylene blue

Mehrdad Hajian [1,2], Mohammad Rostamizadeh [1,2,*], Federico Galli [3]

[1] Department of Chemical Engineering, Sahand University of Technology, Sahand New Town, East Azerbaijan, Iran
[2] Environmental Engineering Research Center, Department of Chemical Engineering, Sahand University of Technology, Sahand New Town, Iran
[3] Département de Génie Chimique et Génie Biotechnologique, 2500, boul. de l'Université, Université de Sherbrooke, Sherbrooke (Québec) J1K 2R1, Canada

Received: 2022-11-09 Accepted: 2022-12-29 Published: 2023-02-08

ABSTRACT

Catalysis for environmental remediation is becoming of paramount importance as industrial and urban activities multiply, and by-products contaminate soils and wastewater. Effluents from industrial and urban activities have led to many environmental problems involving water contamination. Here, we propose a new iron-incorporated metal-organic framework (MOF) photocatalyst to decontaminate water. The nanocatalyst was synthesized by the solvothermal method, and Fe was added to the structure as a promoter and active phase. In this study, we examined the degradation of methylene blue (MB) as a cationic azo dye. The nanocatalysts were characterized by XRD, FE-SEM, BET, NH_3-TPD, and FTIR techniques. The results showed high crystallinity, a large specific surface area, and a uniform promoter distribution. At a pH = 9, a catalyst amount of 110 mg and an initial MB concentration in the effluent of 2 ppm resulted in the highest removal percentage (98 %). The kinetic analysis provided a quasi-first-order model that reasonably matched the experimental data (R^2 = 95 %). The results verified the catalyst's great capability for efficient and fast MB removal in 60 minutes of photocatalytic processing.

Keywords: *Metal-organic framework; Photocatalyst; Wastewater; Dye contaminant*

How to cite this article
Hajian M., Rostamizadeh M, Galli F., Synthesis and characterization of iron incoporated metal-organic framework (MOF) photocatalyst in degradation of methylene blue. J. Water Environ. Nanotechnol., 2023; 8(1):1-12
DOI: 10.22090/jwent.2023.08.001

INTRODUCTION

Effluents from industrial and urban activities have led to many environmental problems involving water contamination. Methylene blue (MB) is one of the colors used in the textile [1], leather [2], paper [3], and plastic [4] industries. So, it is necessary for water purification to research novel and economical procedures. Deposition, evaporation, solvent extraction, electrolysis, reverse osmosis, and membrane separation are just a few of the present wastewater treatment methods [5-10]. These methods are costly and require special equipment, and special waste treatment [11]. Organic dyes make up a wide range of contaminants in textile effluents and related industries. For example, India produced about 77000 tons of organic pigment colors in 2014-2015 [12]. Degrading this type of effluent due to its toxicity and natural resistance to biological and chemical decomposition is, therefore, interesting for companies and society to avoid pollution. The use of active photocatalysts in sunlight, especially in developing countries, is becoming a significant technology in water treatment [13, 14]. Photocatalytic systems complement existing

* Corresponding Author Email: *Rostamizadeh@sut.ac.ir*

methods to remove water pollution [15, 16]. Depending on their structure and band gap, these materials promote electrons in the conductive band either with solar or synthetic ultraviolet light and reduce various chemical and biological pollutants in the climate [14].

Advanced oxidation process includes ultraviolet radiation [17], ultrasound [18], adsorption [19], ozonation [20], Fenton and Fenton-like processes [21], and photocatalytic processes [22, 23], which can be performed with the catalyst, both homogeneously and heterogeneously. Photocatalytic technology with visible light has great potential in water purification and is also one of the most efficient photocatalyst methods [24]. Since solar photocatalyst uses sunlight, this technology is inexpensive, environmentally friendly, and known as a green method. It requires very little equipment and is also suitable for developed countries or remote places without access to electricity. A wide range of semiconductors has been investigated for use in solar energy conversion. This wide range includes monocrystals, polycrystals, amorphous and nanostructured materials in mineral, organic or inorganic-organic forms [25]. Combinatorial porous polymers or materials with a metal-organic structure are crystalline porous materials with high surface area and uniform pore size [26]. Organic dyes are a diverse group of contaminants found in textile and allied industries effluent. Due to their toxicity and resistant character, the degradation of certain types of wastewater has gotten greater attention [27]. Jing et al. [28] investigated the variables that influence photocatalytic degradation of MB and ZIF-8 stability, as well as the kinetics and mechanism involved. The initial MB concentration was 10 mg.L^{-1}, and the initial pH was 6. The amount of ZIF-8 used was 0.5 g.L^{-1}. The result indicated a good degradation efficiency. Wee et al. [29] studied the photodegradation of MB over ZnO, ZIF-8, ZnO@ZIF-8, and P25 using UV light. The result showed that ZnO@ZIF-8, 3 h photodegraded 78 % of MB in MB photodegradation tests, which was equivalent to the commercial Degussa P25 TiO_2 reference catalyst (84 %), and it outperformed pure ZnO (74 %) under identical reaction conditions. Chandra et al. [30] compared the decolorization of methylene blue and rhodamine-B using ZIF-8, TiO_2 nanoparticles (NPs), and TiO_2@ZIF-8. The composite(TiO_2@ZIF-8) has higher photocatalytic activity than TiO_2 NPs for the degradation of methylene blue and rhodamine-B, and it retained high catalytic efficiency even after the fifth catalytic cycle. Yu et al. [31] investigated the photocatalytic performance of core-shell ZnO@ZIF-8 during the photocatalytic degradation of MB under UV irradiation. Karimi et al. [32] studied ZnO/LECA catalyst for the Cr photocatalytic removal in batch photoreactor. They obtained the optimum operation conditions at 0.75 g/L catalyst, pH=5, and Cr initial concentration of 20 ppm. As a result, commercialization challenges and environmental adverse effects in the wastewater treatment process still is problematic. Hekmatshoar et al. [33] reported that ZnO/Bentonit photocatalyst removed 92.5% of 30 mg/L of AR 114 after two hours under UV lamp irradiation. They pointed out that two phenomena have played main roles in the photocatalyst process: (i) formation of the electron-hole mechanism, adsorbing pollutants molecules on the surface of the catalyst; (ii) subsequently adsorbed pollutants reaction with the produced hydroxyl radicals. Shokri et al. [34] also investigated the photodegradation of Ortho-Toluidine (OT) in the presence of TiO_2 in a batch-recirculating reactor. At optimum conditions, the degradation efficiency of OT was 93.5%. Salimi et al. [3a5] studied the degradation of Reactive red 195 (RR195) by UV/ZnO and photo-Fenton processes. The COD removal efficiency in UV/ZnO and photo-Fenton processes was 70.5% (60 min) and 98.5% (20 min), respectively. Mahanpoor et al. [36] investigated the degradation of Acid red 283 (AR 283) by the UV/ZnO process. At optimal conditions, the removal of AR 283 was 99.5% after 60 min. Mphuthi et al. [37] studied the photodegradation of Remazol Brilliant Blue R (RBBR) dye under simulated sunlight irradiation by modified ZIF-8(Zn) and ZIF-67(Co) via metal (Fe^{2+}) exchange. They reported 98% removal of RBBR after 120 min.

To the best of our knowledge, there is no report for MB degradation in photocatalyst reactions over Fe-ZIF-8 nanocatalysts. In this study, the reusable Fe-ZIF-8 nanocatalyst was synthesized and applied for the high efficient and fast MB photocatalytic degradation. The impact of operational conditions on nanocatalyst performance was also investigated.

EXPERIMENTAL

Materials

The reagents were zinc nitrate hexahydrate ($Zn(NO_3)_2.6H_2O$>98wt.%), 2-methylimidazole (Hmim, $C_4H_6N_2$>99wt.%), methanol (CH_3OH>99.5wt.%), Iron (III) nitrate

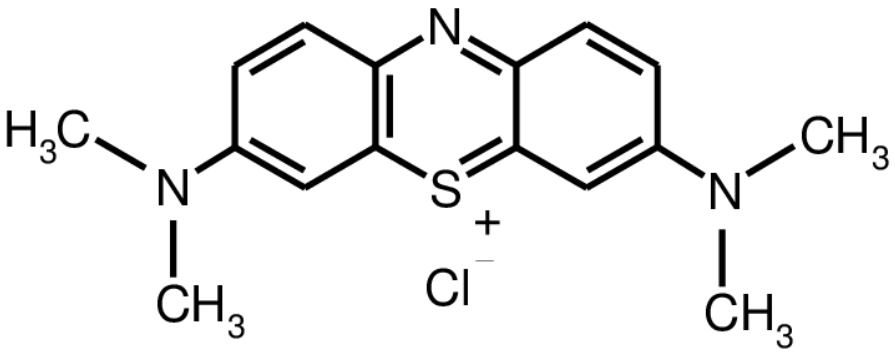

Fig. 1 MB structure

nonahydrate (Fe $(NO_3)_3.9H_2O$>99.8wt.%), N, N-Dimethylformamide (DMF, C_3H_2NO>98wt.%), Ammonia solution (NH_3, 25wt.%) purchased from Merck Company (Germany). MB was purchased from Merck Company (Germany), including the molar mass of 319.85 g mol^{-1}, molecular formula of $C_{16}H_{18}N_3SCL$, and λ_{max} = 665 nm (Fig. 1). Sodium hydroxide (NaOH) and hydrochloric acid (HCl) made by Merck were used to adjust the pH.

Catalyst Preparation

The parent (ZIF-8) nanocatalyst was prepared by the solvothermal method. Zinc nitrate hexahydrate, Iron (III) Nitrate nonahydrate, ammonia, 2-methylimidazole, and *N, N*-Dimethylformamide were all included in the synthesis solution. First, the first solution containing Zinc nitrate hexahydrate, Iron (III) Nitrate nonahydrate, and ammonia was added to the second solution containing 2-methylimidazole and *N, N*-Dimethylformamide at room temperature. The synthesis solution's molar content was $1Zn^{+2}$ /$30NH_3$ /41DMF /2Hmim/$0.12Fe^{2+}$. After mixing for 2 h, the final solution was centrifuged, and the product was washed three times with methanol. Finally, the powder was dried at 100 °C for 12 h. The parent ZIF-8 nanocatalyst was prepared without Fe species.

Catalyst Characterization

X-ray diffraction (XRD) studies were conducted using a D8 Advance Bruker AXS X-ray diffractometer with Ni-filtered Cu K radiation (λ =0.15418 nm). At 40 kV, we detected 2θ deviations in the range of 4–50°. The peak area ratio obtained at 2θ = 7-7.5° was compared to the parent nanocatalyst, called relative crystallinity [38].

In order to determine the morphology and particle size of the synthesized nanocatalysts, FE-SEM images were recorded using the KYKY EM3200 device at a potential difference of 26 kV. Before analysis, some catalyst powder was sprayed onto a metal base and coated twice with gold for 5 minutes. To determine the functional groups on the surface of the synthesized nanocatalyst, FT-IR analysis was performed using the Nicolet Nexus infrared spectroscopy device made in the USA with a resolution of 4 cm^{-1}. For this purpose, a tablet containing 1% by weight of nanocatalyst in KBr powder was prepared as a base for sampling. FT-IR spectra of the nanocatalyst were obtained in the 400–4000 cm^{-1} range. Jenway 6705 UV-vis spectrophotometer was used for spectrophotometer measurements (England). The nitrogen adsorption and desorption isotherms of the catalysts were measured by the nitrogen gas adsorption and desorption method at -196 °C using a USA-made Quantachrome NOVA2000. The BET equation and the nitrogen adsorbed volume at P/P_0= 0.99 determined the total surface area (S_{BET}) and total volume (V_{total}). The total micropore volume (V_{micro}) and the size distribution of pores were calculated using t-plot and BJH (Barrett-Joyner-Halenda) methods, respectively. The mesopore volume (V_{meso}) is the difference between the total calculated and corresponding micropore data. Temperature-programmed desorption of ammonia (NH_3-TPD, Micromeritics, USA) with an online TCD detector analyzed the acidity of the samples. The 53.6 mg of each sample was heated for 4 hours at 550 °C and then saturated with ammonia gas for 1 hour in a micro-reactor. The helium gas stream with a temperature gradient of 10 °C min^{-1} passed over the samples to limit the temperature and desorption between 100 and 700 °C.

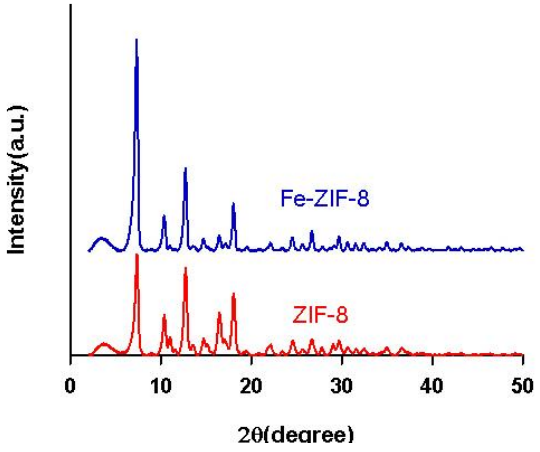

Fig. 2 The XRD patterns of nanocatalysts.

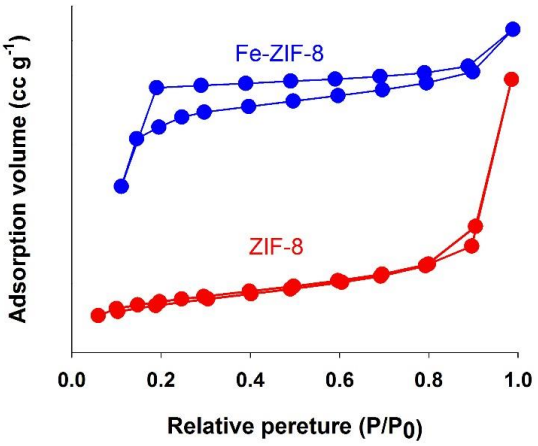

Fig. 3. Nitrogen adsorption/desorption isotherms of ZIF-8 and Fe-ZIF-8a

Table 1. Textural properties of ZIF-8 and Fe-ZIF-8

Sample	S_{BET} ($m^2 g^{-1}$)	V_{Total} ($cm^3 g^{-1}$)	Pore diameter (°A)
ZIF-8	1335	0.64	14
Fe-ZIF-8	614	0.29	17

Photocatalyst process

The synthesized nanocatalysts were applied to improve the MB removal process. The experimental run was carried out in 100 mL of aqueous synthetic wastewater. A 150 W halogen lamp with a visible wavelength (400-700 nm) was placed on top of the reaction vessel. HCl and NaOH adjusted the pH level of the solution for acidic and basic conditions, respectively. The initial MB concentration for all tests was 2 ppm and the reaction mixture was constantly agitated. A spectrometer was used to examine aqueous samples obtained every 5 min at a wavelength of 665 nm. Degradation efficiency was obtained as a percentage of removal based on Equation (1):

$$\%\text{Removal}\,\frac{C0-Ct}{C0}=00$$

C_0 and C_t were the MB concentration in the initial effluent and sample, respectively.

RESULTS AND DISCUSSION

Nanocatalyst characterization

The nanocatalysts contained the MFI structure of ZIF-8 based on the XRD patterns (Fig. 2), which is in line with the literature [39]. Peaks of ZIF-8 are at 2θ = 7.3°,10.3°, 12.6°, 16.5°, 18.0° [38]. In addition to the index peaks, additional peaks in the ZIF-8 structure indicate the presence of crystalline impurities in the ZIF-8 structure. The intensity of the ZIF-8 index peaks in the iron-modified sample has been changed owing to the effects of iron metal on the crystal structure. In the XRD pattern of the Fe-ZIF-8 sample, no indicator peak was observed in 2θ of 29.9, 35.2, 42.8, 53.5, and 56.9°, according to JCPDS 19-629 of iron oxide. The absence of a peak related to iron oxide indicates a strong metal interaction. This uniformity of the metal solution, which is the catalyst's active ingredient, is an advantage for the synthetic catalyst. The increase in peak intensity in the Fe-ZIF-8 sample indicates an increase in crystallinity in the structure compared to the ZIF-8, which is in line with the literature [38, 40].

ZIF-8 shows a type I isotherm with H_4-type hysteresis, including a surface area of 1335 $m^2 g^{-1}$ (Fig. 3). Adding iron to the ZIF-8 structure reduces the specific surface area, pore diameter, and pore volume (Table 1), which is in line with the literature [41]. The microporous structures were indicated by the large adsorption volume at a low relative pressure (P/P_0=0.1) [27]. In contrast, the second adsorption at high relative pressure indicates macro and mesoporous structures formed by the accumulation of nanoparticles.

The NH_3-TPD measurements indicated similar

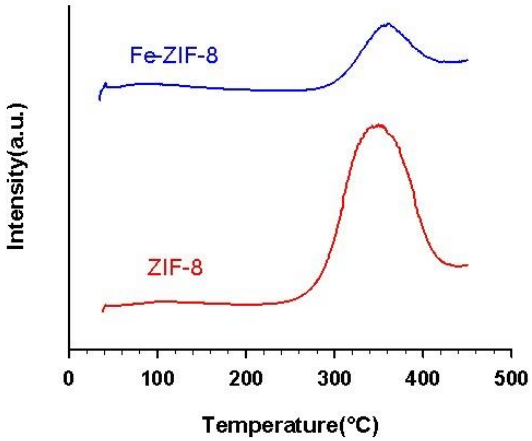

Fig. 4 NH_3-TPD profiles.

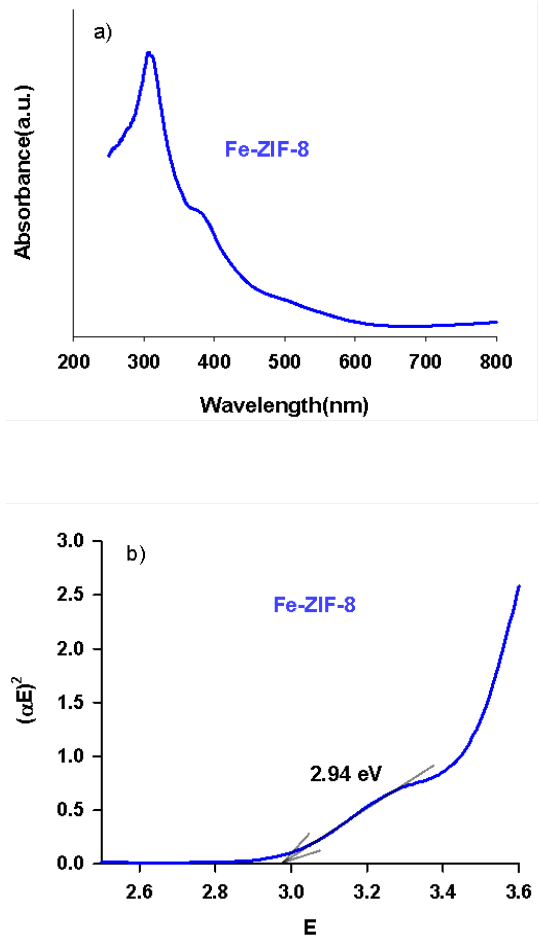

Fig. 5. The DRS results of Fe-ZIF-8 nanocatalyst: **a)** DR-UV–Vis spectrum and **b)** Tauc plot

patterns for the nanocatalysts containing different strengths and amounts of the acid sites (Fig. 4). The two peaks at temperature ranges of 120–300 °C and 310–500 °C characterize the weak and strong acid sites, respectively [42]. The acidity density was calculated from the peak area. The peak area is proportional to the number of acid sites, and the peak temperature shows the acid strength. The parent nanocatalyst involves strong (2.0 NH_3 mmol g^{-1}) and weak (0.05 NH_3 mmol g^{-1}) acid sites. Fe incorporation in the structure reduced the strong acid sites and increased the weak acid sites of the nanocatalyst, resulting in a slightly strong/weak ratio reduction. (Table 2). The total number and intensity of acid sites were considerably reduced. In addition, the peak position shifts to a higher temperature, which indicates the higher strength of strong acid sites in the Fe-ZIF-8 nanocatalyst. This phenomenon can be due to the deposition of iron oxide on the catalyst and the entry of iron oxide into the pores.

Fig. 5a shows UV–Vis diffuse reflection measurement at room temperature. The sample energy band gap was determined by the Tauc method [43]. The curve of $(\alpha E)^2$ versus E was plotted (Fig. 5b), where E is the photon energy and is an absorption coefficient. The results showed an absorption edge around 305 nm, corresponding to an energy band gap of 2.94 eV.

In ZIF-8, the functional groups at wavelengths of 3138 and 2933 cm^{-1} can be assigned to the tensile vibrations of the C-H chain in the methyl group and the imidazole ring (Fig. 6). While the band at 1595 cm^{-1} can be attributed to the C=C chain. The functional groups in the range 1100-1400 cm^{-1} are related to the C-H chain and the wavelength of 421 cm^{-1} is related to the Zn-N tensile vibrations [44].

The morphology of the ZIF-8 nanocatalyst consists of dispersed plate particles, as shown in Fig. 7. The morphology has changed significantly with the addition of iron to the ZIF-8 structure in the form of crowded, lumpy, and uneven particles [38].

Catalytic performance

Effect of the initial amount of MB on effluent

The impact of the initial MB concentration over the Fe-ZIF-8 was investigated using 2, 5, 8, and 11 ppm (Fig. 8) while temperature, agitation, halogen light power, and wavelength and catalyst mass were kept constant (25 °C, 160 rpm, 150 W, 400-700 nm, 1 g L^{-1}, respectively). With increasing MB

Table 2. Acidity and strong/weak ratio.

Catalyst	Acidity (NH_3 mmol g^{-1})			Strong/weak
	Weak	Strong	Total	
ZIF-8	0.05	2.00	2.05	38
Fe-ZIF-8	0.15	0.85	1.00	6

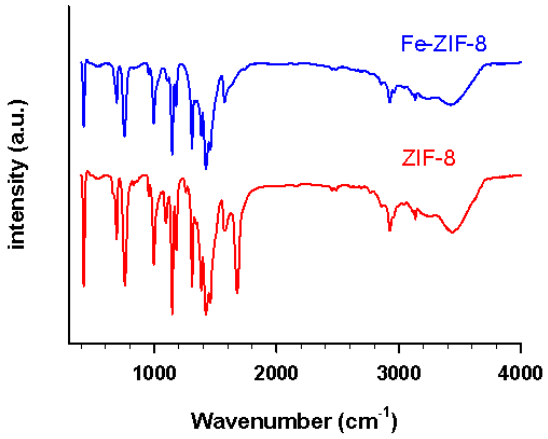

Fig. 6 FT-IR spectrum of the nanocatalysts in the range of 400–4000 cm^{-1}.

concentration, degradation efficiency decreases, which is in agreement with the literature [45]. Indeed, light cannot penetrate the catalyst's surface with the high initial concentration of MB. As a result, light intensity lowered the production of a relative quantity of $^{\bullet}OH$ and $^{\bullet}O_2^-$ on the catalyst surface.

Effect of pH

The pH of the solution impacts the photocatalytic degradation processes because it determines the surface charge characteristics of the photocatalyst [45]. Fig. 9 shows the performance of Fe-ZIF-8 nanocatalyst at various pH levels ranging from 3–11. The electrical repulsion/attraction between MB molecules and the Fe-ZIF-8 nanoparticles can be occurred owing to the ionization phenomena. pHpzc, as the pH at the point of zero charges, is a crucial factor that significantly influences the adsorption behavior of the contaminant molecules and, consequently, photocatalytic degradation. At this pH, the photocatalyst surface charges are neutral. The photocatalyst surface charge is positive when the pH value of the dye solution is lower than pHpzc. When the pH value of the dye solution is lower than pHpzc the photocatalyst surface charge is positive. At pH=3, the MB molecule has a positive ionized state the surface of the nanoparticles has a positive charge (the pH_{PZC} for Fe-ZIF-8 nanoparticles equals 8), so there is a strong electrostatic repulsion between the MB molecules and nanocatalyst particles. By increasing the initial pH of the effluent to 5, the rate of removal increases. The surface charge of nanoparticles and MB is still positive. Still, the strength of these charges was reduced by approaching zero loads, and the high surface area of nanoparticles and van der Waals adsorption mechanisms lead MB molecules closer to the surface of nanoparticles and the reaction is possible.

In the alkaline range, pH = 11 and 9, by changing the surface charge of nanoparticles from positive to negative, electrostatic attraction leads to maximum adsorption of MB molecules to the surface of photocatalytic nanoparticles, and a higher removal percentage is observed. In subsequent tests, due to the slight change in the removal percentage at a pH equal to 11 compared to 9, the optimal pH of the effluent is considered equivalent to 9.

Effect of Fe-ZIF-8 photocatalyst Dosage

The applied amount of catalyst in the photocatalytic process is considered the direct cost of the process. Therefore, to find the optimal amount of Fe-ZIF-8 catalyst, the values of 30, 50, 80, and 110 mg of nanocatalyst were evaluated. As shown in Fig. 10, increasing the concentration of Fe-ZIF-8 catalyst from 30 to 50 mg leads to high dyeing efficiency. However, the subsequent increase in the initial concentration of the catalyst has a negative effect on the removal of MB. This can be explained by the turbidity of the solution and the lack of sufficient light to reach the surface of the photocatalysts. However, the subsequent increase in the number of photocatalysts results in an

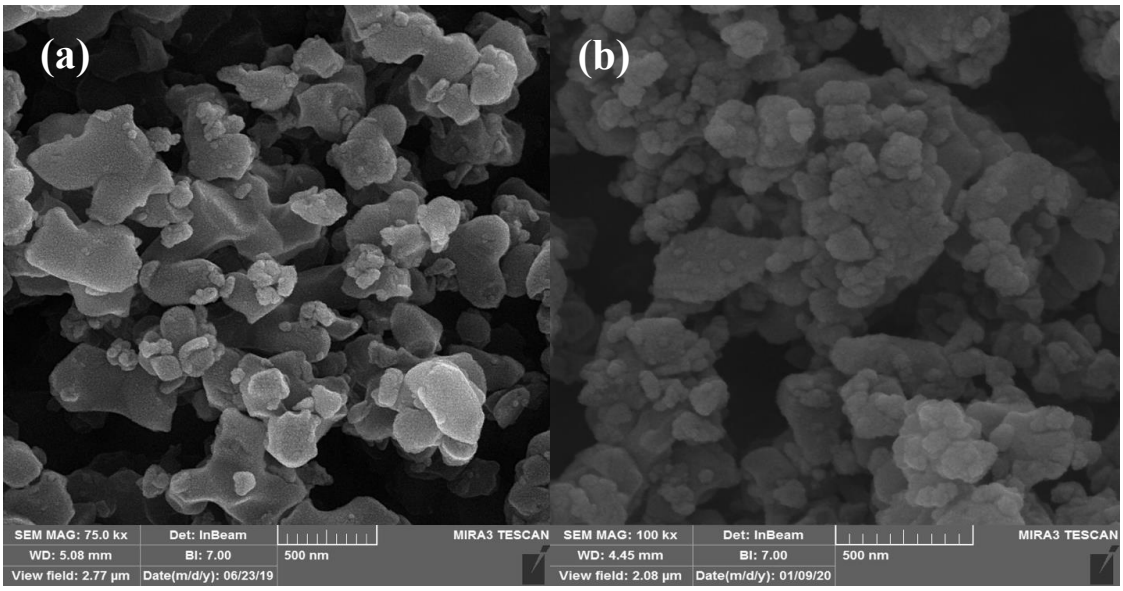

Fig. 7. FE-SEM images of the nanocatalysts (a) ZIF-8 and (b) Fe-ZIF-8.

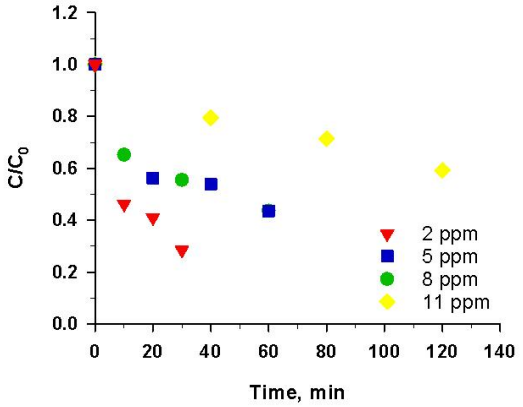

Fig. 8 Influence of different values of initial MB concentration in effluent on MB removal efficiency, Reaction conditions: V= 50 ml, pH=5, 50 mg Fe-ZIF-8 nanocatalyst.

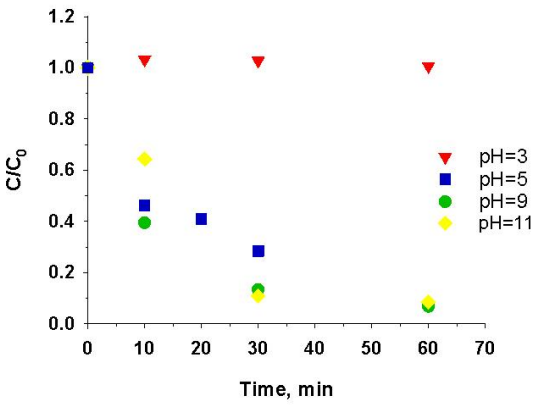

Fig. 9 MB removal efficiency at different solution pH levels. Reaction conditions: V= 50 ml, C_0 =2 ppm, 50 mg Fe-ZIF-8 nanocatalyst.

improvement in the removal rate due to the porous nature of the photocatalyst. The level of 110 mg is selected as the optimal amount of nanocatalyst.

The effect of adsorption

We conducted a dark test (adsorption only) at the optimal operating conditions (pH=9 and 110 mg L^{-1} of nanocatalyst). The results show that adsorption and photolysis role in the MB removal can be ignored compared with the photocatalyst activity (Fig. 11), which highlights the high and efficient performance of the nanocatalyst.

Kinetics of MB removing

In Fe-ZIF-8 nanocatalyst, the LUMO (lowest unoccupied molecular orbital) is generated mainly by empty Zn or Fe orbitals (Fig. 12) [28]. The valance orbitals of Fe provide the larger HOMO (highest occupied molecular orbital) level which causes absorption in the visible region [46]. The kinetic analysis determines the reaction rate, which is crucial for modeling and scale-up applications. To obtain a kinetic model, it is assumed that MB removal is generally obtained according to Equation 11.

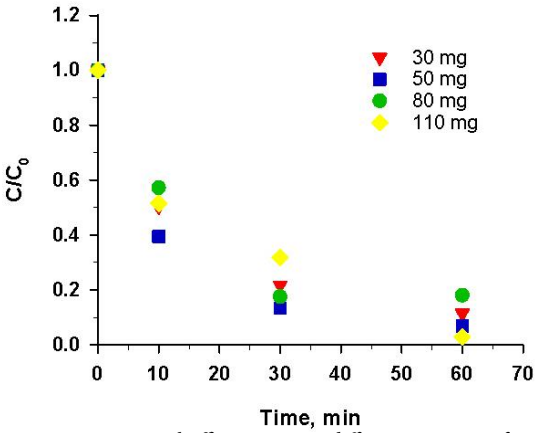

Fig. 10 MB removal efficiency using different amounts of Fe-ZIF-8 nanocatalyst. Reaction conditions: V= 50 ml, C_0 =2 ppm, pH=9.

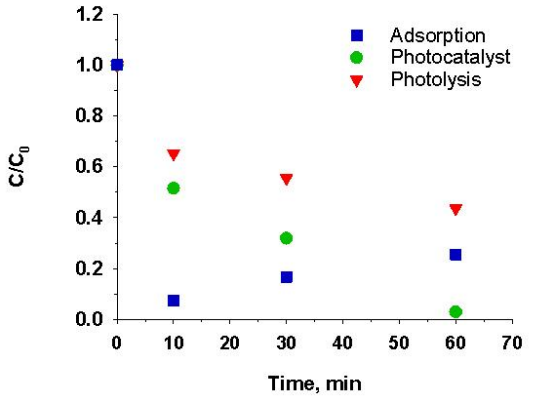

Fig. 11. Different phenomena impact removing MB in optimum operating conditions.

$$MB + OH \rightarrow \text{Oxidized products} \quad (11)$$

Therefore, the intensity of MB removal will be as follows (Equation 12):

$$-\frac{dC}{dt} = kC^* \quad (12)$$

Assuming a high concentration •OH in the reaction medium, by integrating Equation 12, the quasi-first-order kinetics of the photocatalytic system is obtained as follows:

$$\ln(C/C_0) = -kt \quad (13)$$

The residual and initial MB concentrations were C and C_0, respectively, while the •OH concentration was C*. k and t are the rate constant (min^{-1}) and time (min), respectively. The proposed kinetics model shows a high correlation factor with the experimental data (Fig. 13).

According to GC–MS and LC–MS analysis of MB degradation products, they reported that MB can be mineralized after 120 min [47]. A degradation pathway has been developed by identifying intermediate products (especially aromatics), which subsequent hydroxylation results in the opening of the aromatic rings [48].

Scavenger analysis

To investigate the main active species in the MB photocatalytic degradation process over the Fe-ZIF-8 nanocatalyst, radical scavenging experiments were performed. For this purpose, isopropyl alcohol (IPA), triethanolamine (TEA), and para-benzoquinone (p-BQ) were added into the MB solution as the hydroxyl radical (OH), hole (h^+), and superoxide radical ($•O_2^-$) scavengers, respectively. According to the obtained results (Fig. 14), all scavengers reduced the degradation of MB to some extent. The addition of IPA, TEA, and p-BQ decreased the MB degradation from 98% to 18%, 50%, and 74%, respectively. The result of the radical scavenging experiments suggested that the hydroxyl radicals and holes play an important role in the degradation of MB. However, superoxide radicals were also able to degrade the dye to some extent.

Photocatalytic mechanism

Under visible light, the decomposition of color pollutants has a different mechanism called light-sensitive decomposition. In this method, the adsorbed color contaminant has first stimulated by visible light. The excited dye contaminant can inject electrons into the photocatalyst conducting the band and then be trapped by adsorbed O_2. It is noteworthy that if the injected electrons accumulate in the conductive layer, recombination of the electrons and cations produced by the radicals may occur. Therefore, trapping electrons and electron transfer are two essential steps in suppressing the recombination of electrons relative to base dye molecules that are highly unstable. As a result, unstable color dye radicals can be converted to products by reaction with •OH, H_2O, and $•O_2^-$ [45, 49, 50]. The photon-activated surface undergoes a series of chain oxidative–reductive processes, which have been dubbed [14]:

$$\text{photocatalyst} + h\upsilon \rightarrow h^+ + e \quad (1)$$

$$h^+ + H_2O \rightarrow •OH + H^+ \quad (2)$$

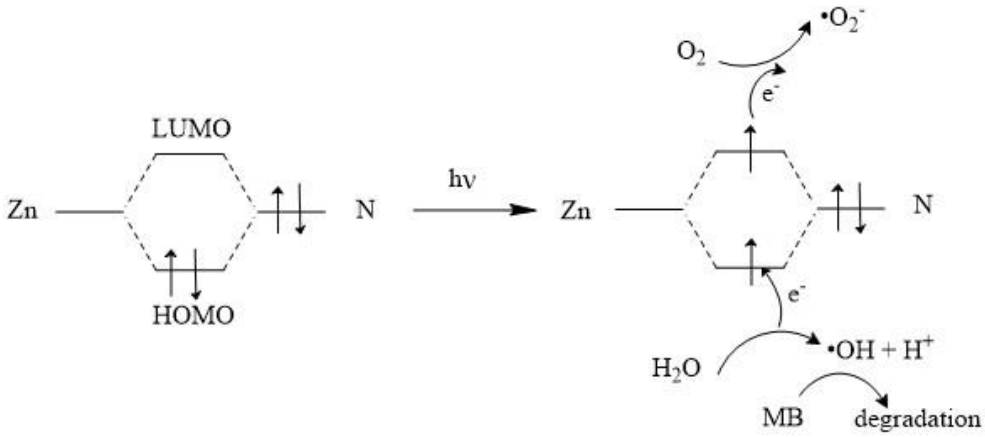

Fig. 12. A simplified model of the photocatalytic reaction mechanism of MB on Fe-ZIF-8.

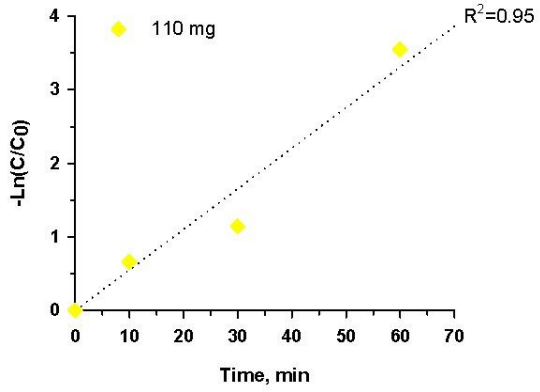

Fig. 13 Kinetics of MB removal in the photocatalytic reaction over Fe-ZIF-8 in the optimum conditions.

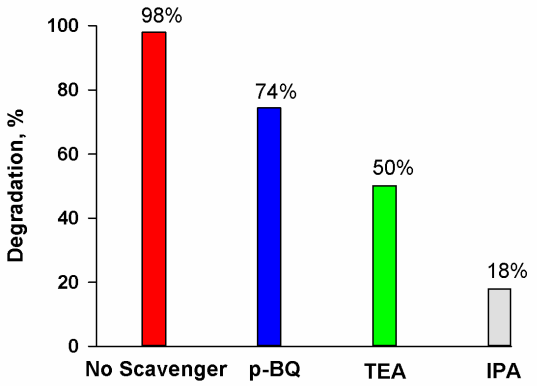

Fig. 14. Influence of IPA, TEA, and p-BQ scavengers on MB photocatalytic degradation over Fe-ZIF-8 nanocatalyst in optimum operating conditions.

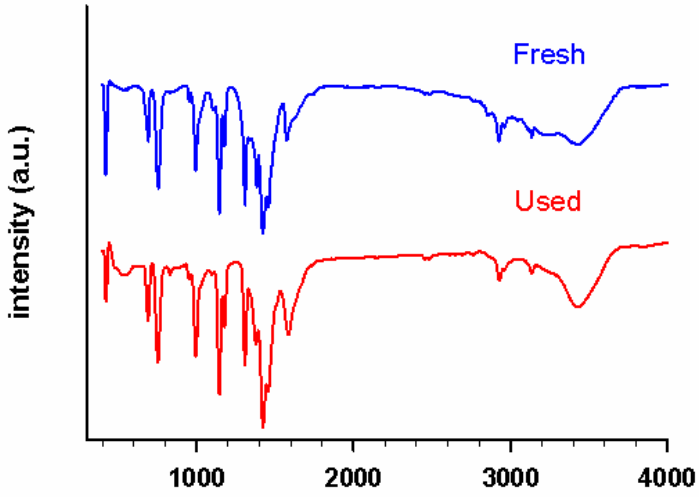

Fig. 15. FT-IR analysis of fresh and spent Fe-ZIF-8 nanocatalysts.

$h^+ + OH^- \rightarrow {}^\bullet OH$ (3)

$h^+ + \text{pollutant} \rightarrow (\text{pollutant})^+$ (4)

$e^- + O_2 \rightarrow {}^\bullet O_2^-$ (5)

${}^\bullet O_2^- + H^+ \rightarrow {}^\bullet OOH$ (6)

${}^\bullet OOH \rightarrow O_2 + H_2O_2$ (7)

$H_2O_2 + {}^\bullet O_2^- \rightarrow {}^\bullet OH + OH^- + O_2$ (8)

$H_2O_2 + h\upsilon \rightarrow 2\ {}^\bullet OH$ (9)

pollutant + (${}^\bullet OH$, h^+, ${}^\bullet OOH$ or ${}^\bullet O_2^-$) → degradation product (10)

Fig. 15 compares the FT-IR results of the fresh and used nanocatalysts. The main peaks remained unchanged, indicating that there was no change in the chemical structure of Fe-ZIF-8. These results demonstrated nanocatalyst reusability and stability in photodegradation processes. The degradation occurred instead of decolorization, and because of the complete removal of dye, the catalyst structure was not affected by MB.

CONCLUSION

This work investigated the photocatalytic degradation of wastewater containing MB by utilizing the Fe-ZIF-8 nanocatalyst. The parent nanocatalyst was prepared via a solvothermal technique, including a Fe metal promoter as the active phase. The characterization of nanocatalysts confirmed the high crystallinity, high specific surface area, and excellent promoter distribution in the nanocatalyst structure. The pH = 9, a catalyst value of 110 mg, and an initial MB concentration of 2 ppm resulted in the highest removal percentage (98%) during 60 min. A quasi-first-order model was provided via kinetic analysis, which was in good agreement with the experimental results (R^2 =95%). Scavenger analysis has shown that OH and h^+ play major roles in the photocatalytic degrading of MB. The Fe-ZIF-8 nanocatalyst showed sufficient stability without significant structure destruction during the reaction. The results confirmed the remarkable potential of the Fe-ZIF-8 nanocatalyst as a photocatalyst for wastewater treatment under visible light.

CONFLICT OF INTEREST

The authors declare no conflict of interest.

REFERENCES

[1] Alinejad, A.;Sadeghi, S.;Ghaderpoori, M.;Sahebi, S.;Ghaderpoury, A.;Mohammadi, A.A.;Saghi, M.H.;Gholampour, Y.;Khani Jeihooni, A., High adsorption of methylene blue from aqueous solutions using leaf-shaped ZIF-8, Int. J. Environ. Anal. Chem., 2021, 101, 2354-2367, 10.1080/03067319.2019.1702170.

[2] Kamaraj, M.;Srinivasan, N.;Assefa, G.;Adugna, A.T.;Kebede, M., Facile development of sunlit ZnO nanoparticles-activated carbon hybrid from pernicious weed as an operative nano-adsorbent for removal of methylene blue and chromium from aqueous solution: extended application in tannery industrial wastewater, Environ. Technol. Innov., 2020, 17, 100540, 10.1016/j.eti.2019.100540. https://doi.org/10.1016/j.eti.2019.100540

[3] Chaukura, N.;Murimba, E.C.;Gwenzi, W., Sorptive removal of methylene blue from simulated wastewater using biochars derived from pulp and paper sludge, Environ. Technol. Innov., 2017, 8, 132-140, 10.1016/j.eti.2017.06.004. https://doi.org/10.1016/j.eti.2017.06.004

[4] Zhou, Y.;Fu, S.;Liu, H.;Yang, S.;Zhan, H., Removal of methylene blue dyes from wastewater using cellulose based superadsorbent hydrogels, Polym Eng Sci., 2011, 51, 2417-2424, 10.1002/pen.22020. https://doi.org/10.1002/pen.22020

[5] Jaspal, D.;Malviya, A., Composites for wastewater purification: A review, Chemosphere, 2020, 246, 125788, 10.1016/j.chemosphere.2019.125788. https://doi.org/10.1016/j.chemosphere.2019.125788

[6] Wang, Y.;Qi, Q.;Fan, J.;Wang, W.;Yu, D., Simple and robust MXene/carbon nanotubes/cotton fabrics for textile wastewater purification via solar-driven interfacial water evaporation, Sep. Purif. Technol., 2021, 254, 117615, 10.1016/j.seppur.2020.117615. https://doi.org/10.1016/j.seppur.2020.117615

[7] Zhang, L.;Lv, P.;He, Y.;Li, S.;Chen, K.;Yin, S., Purification of chlorine-containing wastewater using solvent extraction, J. Cleaner Prod., 2020, 273, 122863, 10.1016/j.jclepro.2020.122863. https://doi.org/10.1016/j.jclepro.2020.122863

[8] Ngah, W.W.;Hanafiah, M.A.K.M., Removal of heavy metal ions from wastewater by chemically modified plant wastes as adsorbents: a review, Bioresour. Technol., 2008, 99, 3935-3948. https://doi.org/10.1016/j.biortech.2007.06.011

[9] Malaeb, L.;Ayoub, G.M., Reverse osmosis technology for water treatment: state of the art review, Desalination, 2011, 267, 1-8, 10.1016/j.desal.2010.09.001. https://doi.org/10.1016/j.desal.2010.09.001

[10] Behboudi, A.;Jafarzadeh, Y.;Yegani, R., Polyvinyl chloride/polycarbonate blend ultrafiltration membranes for water treatment, J. Membr. Sci., 2017, 534, 18-24, 10.1016/j.memsci.2017.04.011. https://doi.org/10.1016/j.memsci.2017.04.011

[11] Sánchez, A.S., Technical and economic feasibility of phosphorus recovery from wastewater in São Paulo's Metropolitan Region, J. Water Process. Eng., 2020, 38, 101537, 10.1016/j.jwpe.2020.101537. https://doi.org/10.1016/j.jwpe.2020.101537

[12] Shanker, U.;Rani, M.;Jassal, V., Degradation of hazardous organic dyes in water by nanomaterials, Environ. Chem. Lett., 2017, 15, 623-642, 10.1016/j.desal.2008.06.004. https://doi.org/10.1007/s10311-017-0650-2

[13] Chong, M.N.;Jin, B.;Chow, C.W.;Saint, C., Recent developments in photocatalytic water treatment technology: a review, Water Res., 2010, 44, 2997-3027, 10.1016/j.watres.2010.02.039. https://doi.org/10.1016/j.watres.2010.02.039

[14] Dong, S.;Feng, J.;Fan, M.;Pi, Y.;Hu, L.;Han, X.;Liu, M.;Sun, J.;Sun, J., Recent developments in heterogeneous photocatalytic water treatment using

visible light-responsive photocatalysts: a review, RSC Adv., 2015, 5, 14610-14630, 10.1039/C4RA13734E https://doi.org/10.1039/C4RA13734E

[15] Schieppati, D.;Galli, F.;Peyot, M.L.;Yargeau, V.;Bianchi, C.L.;Boffito, D.C., An ultrasound-assisted photocatalytic treatment to remove an herbicidal pollutant from wastewaters, Ultrason. Sonochem., 2019, 54, 302-310, https://doi.org/10.1016/j.ultsonch.2019.01.027. https://doi.org/10.1016/j.ultsonch.2019.01.027

[16] Cerrato, G.;Bianchi, C.L.;Galli, F.;Pirola, C.;Morandi, S.;Capucci, V., Micro-TiO2 coated glass surfaces safely abate drugs in surface water, J. Hazard. Mater., 2019, 363, 328-334, https://doi.org/10.1016/j.jhazmat.2018.09.057. https://doi.org/10.1016/j.jhazmat.2018.09.057

[17] Kumar, S.;Ojha, A.K., Oxygen vacancy induced photoluminescence properties and enhanced photocatalytic activity of ferromagnetic ZrO2 nanostructures on methylene blue dye under ultra-violet radiation, J. Alloys Compd., 2015, 644, 654-662, 10.1016/j.jallcom.2015.04.183. https://doi.org/10.1016/j.jallcom.2015.04.183

[18] Karuppusamy, I.;Samuel, M.S.;Selvarajan, E.;Shanmugam, S.;Kumar, P.S.M.;Brindhadevi, K.;Pugazhendhi, A., Ultrasound-assisted synthesis of mixed calcium magnesium oxide (CaMgO2) nanoflakes for photocatalytic degradation of methylene blue, J. Colloid Interface Sci., 2021, 584, 770-778, 10.1016/j.jcis.2020.09.112. https://doi.org/10.1016/j.jcis.2020.09.112

[19] Najafi, M.;Bastami, T.R.;Binesh, N.;Ayati, A.;Emamverdi, S., Sono-sorption versus adsorption for the removal of congo red from aqueous solution using NiFeLDH/Au nanocomposite: Kinetics, thermodynamics, isotherm studies, and optimization of process parameters, J. Ind. Eng. Chem., 2022, 116, 489-503. https://doi.org/10.1016/j.jiec.2022.09.039

[20] Wu, J.;Upreti, S.R., Continuous ozonation of methylene blue in water, J. Water Process. Eng., 2015, 8, 142-150, 10.1016/j.jwpe.2015.10.002. https://doi.org/10.1016/j.jwpe.2015.10.002

[21] Beker, S.A.;Khudur, L.S.;Cole, I.;Ball, A.S., Catalytic degradation of methylene blue using iron and nitrogen-containing carbon dots as Fenton-like catalysts, New J. Chem., 2022, 46, 263-275, 10.1039/D1NJ04761B. https://doi.org/10.1039/D1NJ04761B

[22] Mazhar, S.;Qazi, U.Y.;Nadeem, N.;Zahid, M.;Jalil, A.;Khan, F.;Ul-Hasan, I.;Shahid, I., Photocatalytic degradation of methylene blue using polyaniline-based silver-doped zinc sulfide (PANI-Ag/ZnS) composites, Environ. Sci. Pollut. Res., 2022, 29, 9203-9217, 10.1016/j.jhazmat.2007.04.038. https://doi.org/10.1007/s11356-021-16181-7

[23] Omrani, E.;Ahmadpour, A.;Heravi, M.;Bastami, T.R., Novel ZnTi LDH/h-BN nanocomposites for removal of two different organic contaminants: Simultaneous visible light photodegradation of Amaranth and Diazepam, J. Water Process. Eng., 2022, 47, 102581. https://doi.org/10.1016/j.jwpe.2022.102581

[24] Khandegar, V.;Saroha, A.K., Electrochemical treatment of distillery spent wash using aluminum and iron electrodes, Chin. J. Chem. Eng., 2012, 20, 439-443, 10.1016/S1004-9541(11)60204-8. https://doi.org/10.1016/S1004-9541(11)60204-8

[25] Ouyang, S.;Tong, H.;Umezawa, N.;Cao, J.;Li, P.;Bi, Y.;Zhang, Y.;Ye, J., Surface-alkalinization-induced enhancement of photocatalytic H2 evolution over SrTiO3-based photocatalysts, J. Am. Chem. Soc., 2012, 134, 1974-1977, 10.1021/ja210610h. https://doi.org/10.1021/ja210610h

[26] Maeda, K.;Teramura, K.;Lu, D.;Takata, T.;Saito, N.;Inoue, Y.;Domen, K., Photocatalyst releasing hydrogen from water, Nature, 2006, 440, 295-295, 10.1038/440295a. https://doi.org/10.1038/440295a

[27] Rostamizadeh, M.;Jafarizad, A.;Gharibian, S., High efficient decolorization of Reactive Red 120 azo dye over reusable Fe-ZSM-5 nanocatalyst in electro-Fenton reaction, Sep. Purif. Technol., 2018, 192, 340-347, 10.1016/j.seppur.2017.10.041. https://doi.org/10.1016/j.seppur.2017.10.041

[28] Jing, H.-P.;Wang, C.-C.;Zhang, Y.-W.;Wang, P.;Li, R., Photocatalytic degradation of methylene blue in ZIF-8, RSC Adv., 2014, 4, 54454-54462, 10.1039/C4RA08820D. https://doi.org/10.1039/C4RA08820D

[29] Wee, L.H.;Janssens, N.;Sree, S.P.;Wiktor, C.;Gobechiya, E.;Fischer, R.A.;Kirschhock, C.E.;Martens, J.A., Local transformation of ZIF-8 powders and coatings into ZnO nanorods for photocatalytic application, Nanoscale, 2014, 6, 2056-2060, 10.1039/C3NR05289C. https://doi.org/10.1039/c3nr05289c

[30] Chandra, R.;Mukhopadhyay, S.;Nath, M., TiO2@ ZIF-8: A novel approach of modifying micro-environment for enhanced photo-catalytic dye degradation and high usability of TiO2 nanoparticles, Mater. Lett., 2016, 164, 571-574, 10.1016/j.matlet.2015.11.018. https://doi.org/10.1016/j.matlet.2015.11.018

[31] Yu, B.;Wang, F.;Dong, W.;Hou, J.;Lu, P.;Gong, J., Self-template synthesis of core-shell ZnO@ ZIF-8 nanospheres and the photocatalysis under UV irradiation, Mater. Lett., 2015, 156, 50-53, 10.1016/j.matlet.2015.04.142. https://doi.org/10.1016/j.matlet.2015.04.142

[32] Karimi, S.;Shokri, A., The removal of Hexavalent chromium;(Cr (VI)) by ZnO/LECA as a nano photocatalyst using full factorial experimental design, J Nanoanalysis, 2021, 8, 167-175.

[33] Hekmatshoar, R.;Yari, A.R.;Shokri, A., Using ZnO based on Bentonite as a nano photocatalyst for degradation of Acid Red 114 in synthetic wastewater, J Nanoanalysis, 2020, 7, 282-292.

[34] Shokri, A.;Mahanpoor, K., Removal of Ortho-Toluidine from Industrial Wastewater by UV/TiO2 Process, 2016.

[35] Shokri, A.;Salimi, M.;Abmatin, T., Employing photo Fenton and UV/ZnO processes for removing Reactive red 195 from aqueous environment, Fresenius Environ. Bull., 2017, 26, 1560-1565.

[36] Shokri, A.;Mahanpoor, K., Using UV/ZnO process for degradation of Acid red 283 in synthetic wastewater, Bulg. Chem. Commun., 2018, 50, 27-32.

[37] Mphuthi, L.E.;Erasmus, E.;Langner, E.H., Metal exchange of ZIF-8 and ZIF-67 nanoparticles with Fe (II) for enhanced photocatalytic performance, ACS omega, 2021, 6, 31632-31645. https://doi.org/10.1021/acsomega.1c04142

[38] Thi Thanh, M.;Vinh Thien, T.;Thi Thanh Chau, V.;Dinh Du, P.;Phi Hung, N.;Quang Khieu, D., Synthesis of iron doped zeolite imidazolate framework-8 and its remazol deep black RGB dye adsorption ability, J. Chem., 2017, 2017, 10.1155/2017/5045973. https://doi.org/10.1155/2017/5045973

[39] Zhu, M.;Venna, S.R.;Jasinski, J.B.;Carreon, M.A., Room-temperature synthesis of ZIF-

8: the coexistence of ZnO nanoneedles, Chem. Mater., 2011, 23, 3590-3592, 10.1021/cm201701f. https://doi.org/10.1021/cm201701f

[40] Gao, C.;Chen, S.;Quan, X.;Yu, H.;Zhang, Y., Enhanced Fenton-like catalysis by iron-based metal organic frameworks for degradation of organic pollutants, J. Catal., 2017, 356, 125-132, 10.1016/j.jcat.2017.09.015. https://doi.org/10.1016/j.jcat.2017.09.015

[41] Thanh, M.T.;Thien, T.V.;Du, P.D.;Hung, N.P.;Khieu, D.Q., Iron doped zeolitic imidazolate framework (Fe-ZIF-8): synthesis and photocatalytic degradation of RDB dye in Fe-ZIF-8, J. Porous Mater., 2018, 25, 857-869. https://doi.org/10.1007/s10934-017-0498-7

[42] Xiao, J.-D.;Wang, Q.-N.;Feng, Z.-D.;Tang, S.;Liu, Y.;Li, C., Modulating acid-base properties of ZIF-8 by thermal-induced structure evolution, J. Catal., 2022, 406, 165-173, 10.1016/j.jcat.2021.12.033. https://doi.org/10.1016/j.jcat.2021.12.033

[43] Suwanboon, S.;Amornpitoksuk, P., Preparation and characterization of nanocrystalline La-doped ZnO powders through a mechanical milling and their optical properties, Ceram. Int., 2011, 37, 3515-3521, 10.1016/j.ceramint.2011.06.007. https://doi.org/10.1016/j.ceramint.2011.06.007

[44] Low, Z.-X.;Yao, J.;Liu, Q.;He, M.;Wang, Z.;Suresh, A.K.;Bellare, J.;Wang, H., Crystal transformation in zeolitic-imidazolate framework, Cryst. Growth Des., 2014, 14, 6589-6598, 10.1021/cg501502r. https://doi.org/10.1021/cg501502r

[45] Xie, Y.;Yuan, C.;Li, X., Photosensitized and photocatalyzed degradation of azo dye using Lnn+-TiO2 sol in aqueous solution under visible light irradiation, J. mater. sci. eng., B., 2005, 117, 325-333, 10.1016/j.mseb.2004.12.073. https://doi.org/10.1016/j.mseb.2004.12.073

[46] Liu, X.;Jin, A.;Jia, Y.;Jiang, J.;Hu, N.;Chen, X., Facile synthesis and enhanced visible-light photocatalytic activity of graphitic carbon nitride decorated with ultrafine Fe 2 O 3 nanoparticles, RSC Adv., 2015, 5, 92033-92041, 10.1039/C5RA18466E. https://doi.org/10.1039/C5RA18466E

[47] Malik, A.;Nath, M., Multicore-shell nanocomposite formed by encapsulation of WO3 in zeolitic imidazolate framework (ZIF-8): as an efficient photocatalyst, J. Environ. Chem. Eng., 2019, 7, 103401. https://doi.org/10.1016/j.jece.2019.103401

[48] Houas, A.;Lachheb, H.;Ksibi, M.;Elaloui, E.;Guillard, C.;Herrmann, J.-M., Photocatalytic degradation pathway of methylene blue in water, Appl. Catal. B: Environ., 2001, 31, 145-157. https://doi.org/10.1016/S0926-3373(00)00276-9

[49] Lam, S.-M.;Sin, J.-C.;Abdullah, A.Z.;Mohamed, A.R., Degradation of wastewaters containing organic dyes photocatalysed by zinc oxide: a review, Desalin. Water Treat., 2012, 41, 131-169, 10.1080/19443994.2012.664698. https://doi.org/10.1080/19443994.2012.664698

[50] Qiu, R.;Zhang, D.;Mo, Y.;Song, L.;Brewer, E.;Huang, X.;Xiong, Y., Photocatalytic activity of polymer-modified ZnO under visible light irradiation, J. Hazard. Mater., 2008, 156, 80-85, 10.1016/j.jhazmat.2007.11.114. https://doi.org/10.1016/j.jhazmat.2007.11.114